metals

MDPI

Article

Interfacial Engineering of NCM622 Cathodes by a Li_2O–B_2O_3–Li_2SO_4 Composite Layer for High-Stability Low-Temperature Li Storage

Bin Zhang [1], Qing Yin [1,*], Shouxun Peng [1], Zeyu Zhao [1], Meiyu Shi [1], Xiwen Li [1], Zheng Li [1], Bin Xiao [1], Xiuquan Gu [1], Mingjia Zhi [2], Eugene Chubenko [3], Vitaly Bondarenko [3], Hanna Bandarenka [3] and Yanwei Sui [1,*]

[1] School of Materials and Physics, China University of Mining and Technology, Xuzhou 221116, China
[2] School of Materials Science and Engineering, Zhejiang University, 866 Yuhangtang Road, Hangzhou 310018, China
[3] Faculty of Radioengineering and Electronics, Belarusian State University of Informatics and Radioelectronics, P. Browka Str. 6, 220013 Minsk, Belarus
* Correspondence: qingyin0715@cumt.edu.cn (Q.Y.); suiyanwei@cumt.edu.cn (Y.S.)

Abstract

Low-temperature operation of lithium-ion batteries (LIBs) is severely limited by sluggish Li^+ transport, aggravated interfacial polarization, and structural degradation of layered oxide cathodes. Herein, a multifunctional Li_2O-B_2O_3-Li_2SO_4 composite coating, denoted as LBLS, was constructed on $LiNi_{0.6}Co_{0.2}Mn_{0.2}O_2$ (NCM622) through a simple wet-mixing/calcination strategy. Structural and surface characterizations confirm that the LBLS-derived layer is successfully introduced onto NCM622 while the layered α-$NaFeO_2$ framework is well preserved. Benefiting from the regulated surface chemistry and improved interfacial kinetics, NCM622@LBLS exhibits significantly enhanced electrochemical performance, especially under subzero conditions. At −20 °C, the charge-transfer resistance decreases from 160 Ω for pristine NCM622 to 110 Ω after LBLS modification. Moreover, after 500 cycles at −20 °C, NCM622@LBLS maintains 101.57 mAh g^{-1} with a capacity retention of 80.60%, which compares favorably with representative coated NCM622 cathodes evaluated under comparable subzero conditions. In situ XRD reveals suppressed lattice breathing, while ex situ EIS, DRT and GITT confirm reduced interfacial polarization and faster Li^+ diffusion. Depth-profiling XPS further demonstrates that LBLS promotes an inorganic-reinforced CEI containing Li–O, B–O/B–F, and SO_x-containing species, thereby stabilizing the cathode/electrolyte interface during low-temperature cycling.

Keywords: layered oxide cathode; low-temperature Li-Storage; lithium borate/sulfate coating; depth-resolved CEI chemistry

Check for updates

Academic Editor: Luca Pezzato

Received: 30 June 2026
Revised: 19 July 2026
Accepted: 24 July 2026
Published: 29 July 2026

Copyright: © 2026 by the authors. Licensee MDPI, Basel, Switzerland. This article is an open access article distributed under the terms and conditions of the Creative Commons Attribution (CC BY) license.

1. Introduction

Lithium-ion batteries (LIBs) have been widely used in portable electronics, electric vehicles, and large-scale energy-storage systems owing to their high energy density, long cycle life, and mature manufacturing technology [1–3]. With the rapid development of electric transportation, outdoor energy-storage devices, and energy systems operating in cold regions, stable battery operation under low-temperature conditions has become increasingly important. However, subzero temperatures severely deteriorate the electrochemical reaction kinetics of LIBs [4,5]. The increased electrolyte viscosity, reduced ionic

conductivity, sluggish Li^+ desolvation, slow solid-state diffusion, and slower charge transfer at the electrode/electrolyte interface collectively lead to severe polarization, capacity loss, poor rate capability, and shortened cycle life. Therefore, improving ion-transport kinetics and interfacial stability at low temperature is essential for the development of wide-temperature lithium-ion batteries [6–8].

Among various cathode materials, layered $LiNi_xCo_yMn_{1-x-y}O_2$ cathodes have attracted extensive attention because of their high reversible capacity, relatively high operating voltage, and tunable transition-metal composition [9,10]. In particular, $LiNi_{0.6}Co_{0.2}Mn_{0.2}O_2$, commonly referred to as NCM622, offers a balanced combination of capacity, cost, and structural stability, making it a representative layered oxide cathode for practical lithium-ion batteries [11–13]. Nevertheless, NCM622 still suffers from kinetic, interfacial, and structural degradation under low-temperature conditions [14,15]. Li^+ diffusion within the layered lattice and charge transfer across the cathode/electrolyte interface are strongly hindered, resulting in increased interfacial resistance and limited active-material utilization [16–18]. Meanwhile, the reactive transition-metal–oxygen surface can promote electrolyte decomposition and the accumulation of resistive cathode/electrolyte interphase (CEI) species. In addition, repeated Li^+ extraction/insertion induces anisotropic lattice breathing and local strain accumulation, which further accelerates structural degradation and interfacial instability. Therefore, the low-temperature failure of NCM622 originates from the coupled effects of sluggish kinetics, unstable interfacial chemistry, and structural strain [19,20]. Surface coating has been considered an effective strategy to improve the electrochemical stability of Ni-rich layered cathodes. Conventional oxide, fluoride, phosphate, and polymer coatings can partially suppress the direct contact between the cathode surface and electrolyte, thereby reducing parasitic reactions [21]. However, many inert coating layers possess limited Li^+ transport ability and may introduce additional interfacial resistance, especially under low-temperature conditions. For low-temperature cathodes, an ideal coating layer should not only serve as a protective barrier, but also regulate surface chemistry, facilitate Li^+ migration, suppress interfacial side reactions, and alleviate structural degradation during cycling. Therefore, constructing a multifunctional coating layer with both chemical stability and kinetic compatibility is highly desirable for improving the low-temperature performance of NCM622 [22]. A related multifunctional design principle has also been applied in petroleum processing. Khormali combined complementary corrosion and scale inhibitors in a single formulation to suppress steel corrosion and the precipitation of $CaCO_3$, $BaSO_4$ and $CaSO_4$ through adsorption and inhibition of crystal growth [23]. Although this soluble inhibitor system differs from a solid cathode coating, it illustrates the broader value of integrating distinct chemical functions to address degradation processes.

Lithium sulfate and lithium borate coatings have been shown to suppress interfacial degradation, facilitate lithium ion transport, and improve the structural stability of nickel rich layered cathodes [24–26]. Related multicomponent inorganic modifications have also been developed to combine interfacial protection with ion transport or structural buffering. Nevertheless, the above studies primarily focus on room-temperature, elevated-temperature or high-voltage operation, while the coupled effects of coating chemistry on charge transfer, solid-state Li^+ diffusion, CEI evolution, and anisotropic lattice response under subzero conditions remain insufficiently resolved. Here, a Li_2O–B_2O_3–Li_2SO_4 (LBLS)-derived interfacial layer is constructed on NCM622 and evaluated specifically under low-temperature conditions. The LBLS coating is designed as a multifunctional interfacial regulator rather than a simple inert layer. Lithium borate-related species can stabilize the surface chemistry and suppress excessive electrolyte decomposition [27], while sulfate-related components contribute to the formation of a robust inorganic interfacial environment [28]. Meanwhile, the lithium-containing nature of the coating helps maintain

favorable Li^+ transport across the cathode/electrolyte interface. Through this synergistic design, the LBLS layer is expected to reduce interfacial polarization, improve charge-transfer kinetics, and mitigate structural strain during Li^+ extraction/insertion [29].

Structural and surface characterizations demonstrate that the LBLS layer is successfully introduced onto NCM622 while the layered α-$NaFeO_2$ framework is well preserved. The appearance of B- and S-containing species in XPS and elemental mapping, together with the surface-modified morphology observed by SEM and TEM, confirms the formation of a Li_2O-B_2O_3-Li_2SO_4-derived coating on the cathode particles. Such a surface modification brings a clear improvement in low-temperature electrochemical behavior. At −20 °C, the charge-transfer resistance decreases from 160 Ω for pristine NCM622 to 110 Ω for NCM622@LBLS. More importantly, after 500 cycles at −20 °C, NCM622@LBLS still retains 101.57 mAh g^{-1} with a capacity retention of 80.60%, showing much better cycling durability than pristine NCM622. Representative surface modification strategies for NCM622 cathodes reported recently are quantitatively compared in Table S1, which further highlights the outstanding low-temperature long-term cycling stability enabled by our multifunctional LBLS coating [20,30–35]. The improvement is further supported by the structural and kinetic evolution during cycling. In situ XRD shows that the LBLS coating reduces the movement of the (003) reflection and suppresses the fluctuation of both a- and c-axis lattice parameters, indicating a more moderate lattice response during Li^+ extraction/insertion. Ex situ EIS and DRT results show lower interfacial resistance and weaker polarization over different charge/discharge states, while GITT confirms faster Li^+ diffusion at −20 °C. In addition, depth-profiling XPS after cycling reveals a regulated CEI chemistry, where carbonate-derived decomposition products are suppressed and Li–O, B–O, and SO_4^{2-}-type inorganic species are better incorporated into the interphase. These results suggest that the LBLS coating improves the low-temperature behavior of NCM622 through the combined stabilization of surface chemistry, interfacial charge transfer, and lattice evolution, providing a practical surface-engineering strategy for developing high-performance layered oxide cathodes under subzero conditions.

2. Experimental Section

2.1. Materials

Commercial $LiNi_{0.6}Co_{0.2}Mn_{0.2}O_2$ (NCM622, 99.9%), lithium oxide (Li_2O, 99.9%), boric acid (H_3BO_3, 99.9%), lithium sulfate (Li_2SO_4, 99.9%), ethanol (99.9%), poly (vinylidene fluoride) (PVDF, 99.9%), Super P carbon black, N-methyl-2-pyrrolidone (NMP, 99.9%), Al foil, polypropylene separators, and lithium foil were purchased from Dodo Chem Co. and used without further purification. Propylene carbonate (PC, 99.95%, battery grade), 1,2-dimethoxyethane (DME, 99.95%, battery grade), isobutyl acetate (iBA, 99.9%, anhydrous), lithium tetrafluoroborate ($LiBF_4$, 99.9%), lithium bis(fluorosulfonyl)imide (LiFSI, 99.9%), and lithium difluoro(oxalato)borate (LiDFOB, 99.9%) were also obtained from Dodo Chem Co (Hefei, China). The LBLS-coated NCM622 cathode material was prepared through a wet-mixing/calcination method. To optimize the nominal LBLS loading, NCM622 samples coated with 1, 3 and 5 wt% LBLS relative to the mass of NCM622 were evaluated for 100 cycles at −20 °C under identical conditions. As shown in Figure S1, the 3 wt% sample exhibited the highest reversible capacity and capacity retention at −20 °C and was therefore selected for the subsequent experiments. The inferior performance at lower and higher loadings suggests that an intermediate coating content provides sufficient surface modification without introducing an excessive interfacial transport penalty. For the optimized NCM622@LBLS sample, the nominal coating composition was 32.5 wt% Li_2O, 57.5 wt% B_2O_3, and 10 wt% Li_2SO_4. Accordingly, 9.75 mg of Li_2O, 30.64 mg of H_3BO_3, and 3.00 mg of Li_2SO_4 were dispersed in 20 mL of ethanol, followed by high-speed homogeniza-

tion for 30 min to obtain a uniform precursor suspension. Subsequently, 1.0 g of NCM622 powder was added into the above suspension and continuously homogenized to ensure the homogeneous distribution of the coating precursors on the particle surface. The ethanol was then slowly evaporated in a 60 °C water bath under continuous stirring. The obtained dry precursor powder was calcined at 500 °C for 10 h under a flowing oxygen atmosphere, followed by natural cooling to room temperature, to form the Li_2O-B_2O_3-Li_2SO_4 composite coating. The coated sample was denoted as NCM622@LBLS. For comparison, pristine NCM622 was subjected to the same thermal treatment under identical conditions but without adding LBLS precursors and was used as the control sample. The low-temperature electrolyte was prepared by dissolving 0.75 M $LiBF_4$, 0.2 M LiFSI, and 0.05 M LiDFOB in PC:DME:iBA mixed solvent with a volume ratio of 25:65:10. Cathode slurries were prepared by mixing the active material, PVDF, and Super P carbon black at a mass ratio of 8:1:1 in NMP. The slurry was cast onto Al foil, dried under vacuum at 100 °C for 8 h, and punched into 12 mm disks. CR2032-type Li||NCM622 and Li||NCM622@LBLS coin cells were assembled in an Ar-filled glove box with H_2O and O_2 contents below 0.1 ppm, using 150 μL electrolyte per cell. The cells were cycled between 2.5 and 4.5 V using a Neware BTS-4000 battery tester, and EIS measurements were recorded from 0.01 Hz to 1 MHz with a 5 mV perturbation. The current density corresponding to 1 C was defined as 276 mA g^{-1} based on the theoretical capacity of NCM622. Galvanostatic intermittent titration technique (GITT) measurements were performed using a LAND CT3002AU battery testing system within a voltage window of 2.5–4.5 V. The cells were galvanostatically charged/discharged at 0.1 C (27.6 mA g^{-1}) with a current pulse of 10 min, followed by an open-circuit relaxation period of 60 min to allow the cell voltage to approach equilibrium. Galvanostatic cycling and rate capability measurements were independently repeated using more than five separately assembled coin cells for each sample and testing condition.

2.2. Characterizations

The crystal structures of pristine NCM622 and NCM622@LBLS were characterized by X-ray diffraction (The XRD, Bruker D8 ADVANCE was purchased from Bruker Beijing Scientific Technology Co., Ltd., Beijing, China) with Cu Kα radiation operated at 40 kV and 40 mA. The diffraction patterns were collected over a 2θ range of 10–70° with a step size of 0.02°. The surface morphology and microstructure of the pristine and coated cathode materials were examined using field-emission scanning electron microscopy (The FE-SEM, Hitachi SU8220 was purchased from Hitachi High-Tech Science (Beijing) Co., Ltd., Beijing, China). Before SEM observation, the samples were sputter-coated with a thin Au layer to improve electrical conductivity. After electrochemical cycling, the coin cells were disassembled in an Ar-filled glove box. The cycled NCM622 and NCM622@LBLS cathodes were gently rinsed with anhydrous DME to remove residual electrolyte and then dried under vacuum. The surface morphologies of the cycled electrodes were observed by FE-SEM operated at 5 kV and 10 μA. X-ray photoelectron spectroscopy (The XPS, ULVAC-PHI VersaProbe 4 was purchased from ULVAC Trading (Shanghai) Co., Ltd., Shanghai, China, Al Kα radiation, 1486.6 eV) was employed to analyze the surface chemical compositions and interfacial species of the pristine and cycled cathodes. All XPS spectra were calibrated using the adventitious C 1s peak at 284.8 eV and processed with CasaXPS2.3.25 software.

3. Results and Discussion

3.1. Characterization

As shown in Figure 1a, the XRD patterns of pristine NCM622 and modified NCM622@LBLS exhibit highly similar diffraction features, and all the main reflections can be well indexed to the typical layered α-$NaFeO_2$ structure with rhombohedral symme-

try. The characteristic diffraction peaks corresponding to the (003), (101), and (104) planes are clearly preserved after LBLS modification, indicating that the bulk layered framework of NCM622 remains intact and that the surface treatment does not destroy the host crystal structure. In addition, no obvious impurity peaks are detected for NCM622@LBLS, suggesting that the introduced LBLS phase does not form detectable crystalline byproducts, which is likely related to its low content and low crystallinity on the particle surface. Notably, compared with pristine NCM622, the diffraction intensity of NCM622@LBLS becomes relatively weaker after modification. This phenomenon can be attributed to the formation of a surface LBLS layer composed of Li_2O-B_2O_3-Li_2SO_4, which may possess low crystallinity or partial amorphous characteristics and thus weaken the diffraction response of the underlying NCM622 phase. At the same time, the interfacial interaction between the LBLS layer and the NCM622 surface may introduce local lattice distortion and microstrain, leading to a decrease in peak intensity while preserving the overall layered structure. Furthermore, the enlarged view of the (003) reflection in Figure S2 reveals that the peak position shifts from 18.71° for pristine NCM622 to 18.92° for NCM622@LBLS after modification. Correspondingly, the interlayer spacing decreases from 4.73 to 4.68 Å, indicating a slight contraction of the lattice along the c-axis direction. Such a shift suggests that the LBLS treatment alters the local crystal environment of the surface region through interfacial chemical interaction, resulting in a more compact layered arrangement. Combined with the absence of impurity peaks, these results demonstrate that the LBLS modification effectively tailors the surface structural characteristics of NCM622 while maintaining its bulk phase integrity.

X-ray photoelectron spectroscopy (XPS) was employed to investigate the surface chemical composition and electronic states of pristine NCM622 and NCM622@LBLS. As shown in the survey spectra in Figure S3, both samples exhibit the characteristic signals of Ni, Co, Mn, and O, while additional B and S signals appear after LBLS treatment, confirming the successful construction of an LBLS-derived surface layer on NCM622. Consistent with the survey spectra, the high-resolution B 1s and S 2p spectra of NCM622@LBLS display a B 1s peak at 192.0 eV and a S 2p doublet at 169.5 and 170.4 eV, which can be assigned to B–O species and sulfate-like sulfur species, respectively. These features verify that the Li_2O-B_2O_3-Li_2SO_4-derived components are effectively introduced into the surface region of NCM622. For pristine NCM622, the Ni $2p_{3/2}$ components at 854.38 and 855.61 eV are assigned to Ni^{2+} and Ni^{3+}, while the Ni $2p_{1/2}$ components appear at 871.89 and 873.15 eV, respectively. After LBLS modification, the corresponding Ni $2p_{3/2}$ peaks evolve to 854.39 and 855.77 eV, and the Ni $2p_{1/2}$ peaks shift to 871.65 and 872.93 eV. More importantly, the Ni^{2+}/Ni^{3+} area ratio in the Ni $2p_{3/2}$ region increases markedly from 0.72 to 2.13 after LBLS treatment, indicating a clear enrichment of lower-valence Ni species in the near-surface region. The Co 2p spectra show a similar surface-regulation effect. In pristine NCM622, the Co $2p_{3/2}$ components at 780.0 and 781.6 eV can be assigned to Co^{3+} and Co^{2+}, and the corresponding Co $2p_{1/2}$ peaks are located at 795.0 and 797.3 eV. After LBLS treatment, the Co^{3+} $2p_{3/2}$ peak remains at about 780.0 eV, whereas the Co^{2+} $2p_{3/2}$ component shifts to 783.0 eV, accompanied by a change in the Co $2p_{1/2}$ Co^{2+} component from 797.3 to 796.8 eV. Meanwhile, the Co^{2+}/Co^{3+} area ratio increases from 1.72 to 3.62, implying that Co also participates in the interfacial charge-compensation process induced by the LBLS layer. Such a redistribution of surface Co valence is expected to moderate the oxidative reactivity of the near-surface transition-metal–oxygen network and contribute to interfacial stabilization, together with the Ni valence adjustment. By comparison, the Mn 2p peaks at 642.4 and 653.9 eV remain characteristic of Mn^{4+}, suggesting that the Mn framework is largely preserved after surface modification. The O 1s spectra were further analyzed to clarify the surface oxygen environment of pristine NCM622 and NCM622@LBLS (Figure S4). For

pristine NCM622, the O 1s spectrum is mainly composed of the lattice oxygen component from the transition-metal–oxygen framework (Me–O) and a higher-binding-energy oxygen component associated with surface C=O species. After LBLS modification, the O 1s spectrum of NCM622@LBLS exhibits three distinguishable components located at 529.05, 531.40, and 532.30 eV, which are assigned to Me–O, C=O-related oxygen species, and B–O species, respectively. Compared with pristine NCM622, the Me–O contribution is markedly weakened after LBLS coating, while the high-binding-energy oxygen components become dominant. In particular, the appearance of the B–O signal at 532.30 eV confirms the successful introduction of borate-related species from the LBLS coating layer. Meanwhile, the enhanced C=O component at 531.40 eV indicates the presence of carbonate-related oxygen-containing species on the modified surface. These results demonstrate that LBLS modification effectively reconstructs the surface oxygen environment of NCM622 by forming an oxygen-rich borate-containing coating layer, while the retained Me–O signal suggests that the transition-metal–oxygen framework of the layered oxide core remains detectable.

Field-emission scanning electron microscopy (FESEM) was used to examine the morphological features of pristine NCM622 and NCM622@LBLS. As shown in Figures 1g,h and S5, both samples retain their typical spherical secondary-particle morphology, indicating that the LBLS treatment does not destroy the integrated particle structure of NCM622. However, an obvious difference can be observed in the surface texture of the two samples. The pristine NCM622 particle in Figure 1g exhibits a relatively rough surface composed of numerous small and fragmented granular features, suggesting clearly exposed primary-grain boundaries on the particle exterior. After LBLS modification, the particle surface becomes noticeably smoother, and several larger surface protrusions can be observed, as shown in Figure 1h. This morphological evolution suggests that the Li_2O-B_2O_3-Li_2SO_4-derived species are deposited onto the outer surface of NCM622, partially covering the fine surface grains and leading to the formation of a more continuous surface-modified layer. To further clarify the elemental distribution of the modified sample, scanning transmission electron microscopy combined with energy-dispersive X-ray spectroscopy (STEM-EDS) mapping was carried out, as shown in Figure 1i. The elemental maps reveal that Ni, Co, and Mn are uniformly distributed throughout the particle, consistent with the homogeneous composition of the layered NCM622 host. Meanwhile, B and S signals are clearly detected in the modified sample and are distributed over the observed particle region together with O, confirming the successful introduction of LBLS-derived species.

To directly visualize the local surface structure of NCM622@LBLS, aberration-corrected transmission electron microscopy was carried out, as shown in Figure 1j–m. A distinct outer region with contrast different from that of the crystalline interior can be clearly observed along the particle edge in Figure 1j,l, indicating the formation of an LBLS-derived interfacial layer on the surface of NCM622. This surface region is continuously attached to the particle exterior, suggesting that the modification is effectively established at the outermost part of the cathode particles. Further structural details are revealed in Figure 1k,m, where well-resolved lattice fringes are still clearly visible in the inner region beneath the surface layer, demonstrating that the crystalline framework of NCM622 remains well preserved after LBLS treatment. The enlarged images from regions I and II show interplanar spacings of 0.477 and 0.248 nm, which can be indexed to the (003) and (101) planes, respectively, confirming that both the characteristic layered arrangement and the in-plane crystal framework of NCM622 are retained after surface modification. To further verify the local crystallographic ordering, the corresponding fast Fourier transform and inverse fast Fourier transform analyses of the selected regions are provided in Figures S6 and S7. The FFT patterns exhibit distinct diffraction spots, indicating clear lattice periodicity and good local crystallinity in the analyzed domains. Meanwhile, the reconstructed inverse FFT images display parallel and continuous lattice fringes, further supporting the assignment of the

observed lattice spacings and confirming the ordered stacking structure in the crystalline bulk. These results collectively demonstrate that the structural reconstruction induced by LBLS is mainly confined to the outermost surface region, while the crystalline layered bulk of NCM622 remains intact. Such a surface-modified and crystalline-bulk configuration is favorable for electrochemical cycling, because the outer interfacial layer can help alleviate parasitic surface reactions, whereas the preserved layered interior maintains the structural integrity and ion-transport framework of the host cathode. This structure, featuring a modified surface area and a well-preserved crystal core, combines both surface stability and the integrity of the core structure. The outer modified layer helps stabilize the particle surface, while the well-preserved layered interior maintains the inherent crystal framework of the main cathode. This synergistic structural property is expected to contribute to maintaining stable electrochemical performance during the cycling process. Having confirmed the successful construction of the LBLS-derived surface layer and the preservation of the layered NCM622 bulk structure, the electrochemical consequences of this surface modification were further evaluated under both room-temperature and low-temperature conditions. A representative HRTEM image (Figure S8) clearly distinguishes the crystalline bulk NCM622 and amorphous LBLS surface film, where the average coating thickness reaches about 1.64 nm.

3.2. Electrochemical Performance

In order to verify the influence of the LBLS coating structure on the stability of the electrode interface and the kinetics of low-temperature charge transfer, using lithium sheets as the negative electrode, a mixed lithium salt electrolyte composed of $LiBF_4$, LiFSI and LiDFOB (with PC, DME and iBA as solvents) was employed to systematically investigate the electrochemical behavior of the pristine NCM622 and NCM622@LBLS half-cells within the voltage range of 2.5–4.5 V. As shown by the electrochemical impedance spectroscopy curves in Figure 2a,b, NCM622@LBLS exhibits a distinctly smaller semicircle than pristine NCM622 at both 25 °C and −20 °C, indicating a lower charge-transfer resistance. The fitted resistance values summarized in Figures S9 and S10 further confirm this trend. At 25 °C, the charge-transfer resistance decreases from 104 Ω for pristine NCM622 to 70 Ω for NCM622@LBLS, corresponding to a reduction of about 32.7%, and the resistance of pristine NCM622 is approximately 1.49 times that of the modified sample. When the temperature is lowered to −20 °C, the charge-transfer resistance of pristine NCM622 further increases to 160 Ω, whereas that of NCM622@LBLS remains at 110 Ω. This corresponds to a reduction of about 31.3% after LBLS modification, and the absolute resistance difference enlarges from 34 Ω at 25 °C to 50 Ω at −20 °C, indicating that the kinetic advantage of the modified sample becomes more prominent under harsher low-temperature conditions. The reduced interfacial resistance of NCM622@LBLS can be reasonably attributed to the synergistic effect of the LBLS-derived surface layer. On the one hand, the Li_2SO_4 and lithium borate-related species help construct a more stable cathode/electrolyte interfacial environment and suppress excessive parasitic reactions at the particle surface. On the other hand, the surface reconstruction induced by LBLS treatment can lower the charge-transfer barrier at the cathode interface, thereby alleviating interfacial polarization during cycling. As a result, NCM622@LBLS is expected to exhibit more favorable electrochemical kinetics and improved low-temperature electrochemical performance.

To further evaluate the charge-storage kinetics associated with LBLS modification, CV measurements were conducted over the scan-rate range of 0.1–0.5 mV s^{-1}. As shown in Figure 2c,d, both pristine NCM622 and NCM622@LBLS exhibit typical redox responses of layered NCM622 cathodes, corresponding to the reversible Li^+ extraction/insertion process. With increasing scan rate, the peak currents gradually increase, accompanied by

a certain degree of peak displacement, which is a common feature caused by enhanced polarization under faster electrochemical perturbation. Therefore, the CV profiles suggest that LBLS modification does not alter the fundamental redox reaction of NCM622, while the difference in kinetic behavior needs to be further clarified by quantitative analysis.

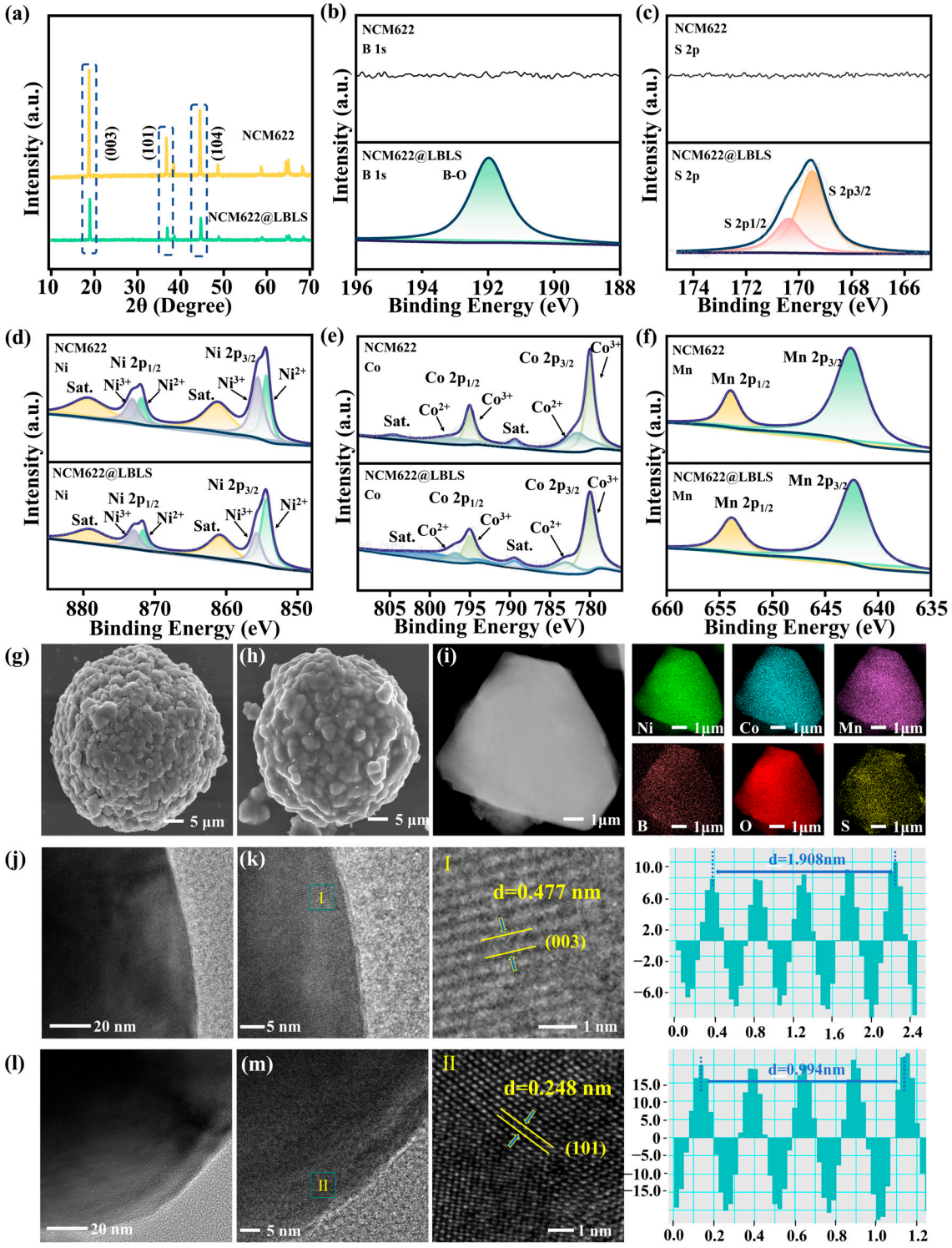


Figure 1. (**a**) XRD patterns of pristine NCM622 and NCM622@LBLS. XPS spectra of (**b**) B 1s, (**c**) S 2p, (**d**) Ni 2p, (**e**) Co 2p and (**f**) Mn 2p. FESEM images of (**g**) pristine NCM622 and (**h**) NCM622@LBLS. (**i**) STEM-EDS elemental mappings of NCM622@LBLS. (**j**,**l**) TEM images and (**k**,**m**) HRTEM images (inset: magnified lattice spacing and corresponding inverse FFT images) of NCM622@LBLS.

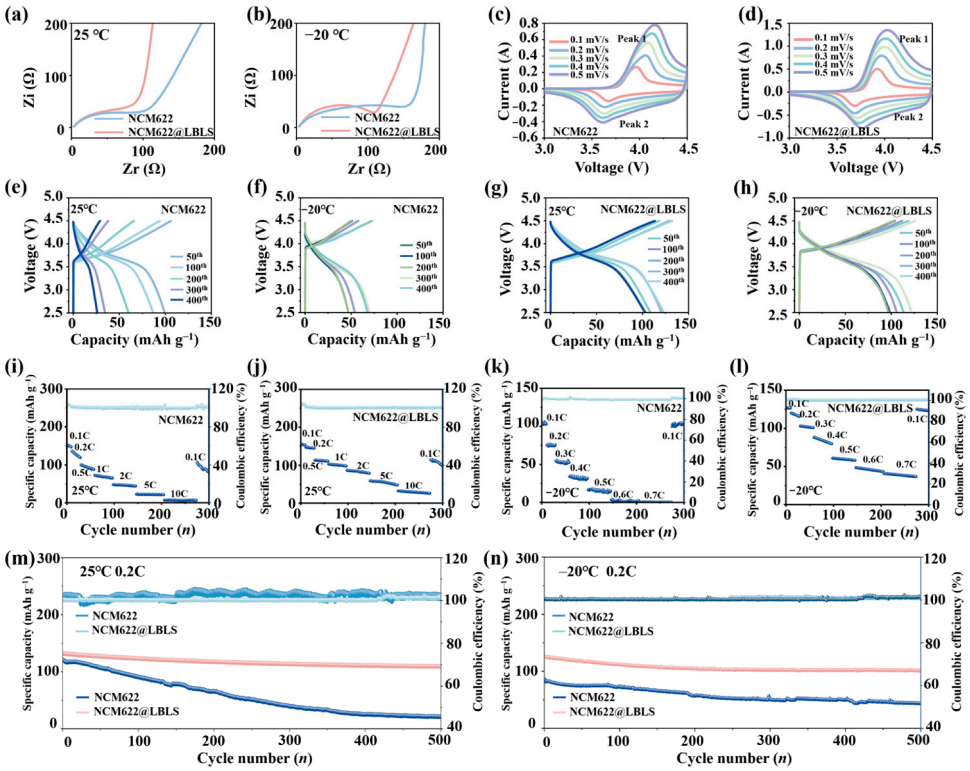


Figure 2. EIS spectra of both pristine NCM622 and NCM622@LBLS cathodes recorded at (**a**) 25 °C and (**b**) −20 °C. (**c**,**d**) CV curves at different scan rates. (**e**–**h**) Charge–discharge profiles at (**e**,**g**) 25 °C and (**f**,**h**) −20 °C over selected cycles. (**i**–**l**) Rate capabilities at (**i**,**j**) 25 °C and (**k**,**l**) −20 °C. Long-term cycling performance of both pristine NCM622 and NCM622@LBLS cathodes at (**m**) 25 °C and (**n**) −20 °C.

To quantitatively evaluate the charge-storage behavior, the relationship between peak current and scan rate was analyzed using the power-law equation [36]:

$$i = av^b \tag{1}$$

where i is the peak current, v is the scan rate, and a and b are adjustable parameters. In general, a b value close to 0.5 indicates a diffusion-controlled process, whereas a b value approaching 1.0 suggests a surface-controlled capacitive process. As shown in Figure S11, the calculated b values of pristine NCM622 are 0.62 and 0.58 for the representative redox peaks, indicating that its electrochemical reaction is mainly governed by diffusion-controlled behavior with partial surface contribution. In comparison, NCM622@LBLS exhibits higher b values of 0.69 and 0.62, suggesting an increased surface-controlled kinetic contribution after LBLS modification. This result indicates that the LBLS-derived surface layer helps regulate the reaction pathway at the cathode/electrolyte interface without changing the intrinsic Li^+ insertion/extraction mechanism of the layered host.

Subsequently, the surface-controlled capacitive contribution and diffusion-controlled contribution were further distinguished according to the following relationship [37]:

$$i = k_1 v + k_2 v^{1/2} \tag{2}$$

where $k_1 v$ represents the surface-controlled capacitive contribution and $k_2 v^{1/2}$ corresponds to the diffusion-controlled contribution. Based on this analysis, the capacitive contribution of pristine NCM622 increases from 70% at 0.1 mV s^{-1} to 88% at 0.5 mV s^{-1} (Figure S12), indicating that the surface-controlled process becomes more significant at higher scan rates.

NCM622@LBLS shows consistently higher capacitive contributions of 78%, 83%, 85%, 86%, and 89% over the same scan-rate range, especially at low and intermediate scan rates. This comparison demonstrates that LBLS modification increases the proportion of fast surface-related charge storage and reduces the dependence of the overall reaction on slow solid-state diffusion.

The galvanostatic charge–discharge profiles shown in Figure 2e–h further demonstrate the beneficial effect of LBLS modification on the electrochemical behavior of NCM622. For pristine NCM622, the charge–discharge curves at both 25 °C and −20 °C progressively shift during cycling, accompanied by obvious capacity decay and enlarged voltage hysteresis, indicating increased polarization and deteriorated reaction kinetics. In contrast, NCM622@LBLS exhibits much more stable charge–discharge behavior at both temperatures. As shown in Figure 2g,h, the modified electrode maintains higher reversible capacity and more overlapping voltage profiles from the 50th to the 400th cycle, reflecting improved electrochemical reversibility and suppressed polarization during prolonged cycling. This advantage becomes more pronounced under low-temperature conditions. Even at −20 °C, NCM622@LBLS still retains relatively clear and stable charge–discharge plateaus, whereas pristine NCM622 undergoes much faster capacity attenuation and more severe profile distortion. These results suggest that the LBLS-derived surface layer can effectively stabilize the cathode/electrolyte interface and maintain more favorable charge-transfer kinetics during cycling. More importantly, such interfacial stabilization is particularly beneficial at low temperature, where sluggish charge transfer and aggravated polarization usually dominate the electrochemical response, thereby enabling NCM622@LBLS to deliver more stable low-temperature electrochemical performance.

The rate capability results further confirm that LBLS modification improves the electrochemical performance of NCM622 over the entire tested temperature range, while the beneficial effect becomes much more pronounced under low-temperature conditions. At 25 °C, as shown in Figure 2i and Figure 2j, NCM622@LBLS delivers consistently higher discharge capacities than pristine NCM622 throughout the rate range from 0.1 C to 10 C, giving 155.6, 147.2, 113.3, 102.9, 86.6, 59.2 and 31.9 mAh g^{-1}, respectively, compared with 150.3, 133.1, 100.2, 72.8, 48.4, 22.5 and 7.0 mAh g^{-1} for bare NCM622. The performance gap gradually widens with increasing current density, and the capacity advantage of NCM622@LBLS reaches 1.41 times at 1 C, 1.79 times at 2 C, 2.63 times at 5 C, and 4.56 times at 10 C, indicating that the LBLS-derived surface layer can effectively mitigate polarization accumulation and maintain faster reaction kinetics at high rates. Under −20 °C conditions, the rate capability comparison shown in Figure 2k,l demonstrates a much more pronounced advantage of the LBLS coating. Pristine NCM622 only delivers 103.7, 75.4, 54.7, 34.2, 16.5, 3.4 and 0.5 mAh g^{-1} from 0.1 C to 0.7 C, whereas NCM622@LBLS retains much higher capacities of 126.6, 115.7, 103.1, 88.3, 61.0, 48.7 and 41.0 mAh g^{-1} under the same conditions. The corresponding capacity advantage increases from 1.22 times at 0.1 C to 1.53, 1.88, 2.58 and 3.70 times at 0.2 C, 0.3 C, 0.4 C and 0.5 C, respectively, and further rises sharply to 14.3 times at 0.6 C. When the current density returns to 0.1 C, NCM622@LBLS still recovers to 125.0 mAh g^{-1}, exceeding the 100.0 mAh g^{-1} of pristine NCM622, which further reflects its better reversibility and structural robustness during repeated rate cycling. The enhanced rate performance of NCM622@LBLS can be reasonably attributed to the LBLS-derived surface layer, which stabilizes the cathode/electrolyte interface and reduces the charge-transfer resistance. Meanwhile, the lithium-containing borate and sulfate species in the coating help construct a more favorable interfacial environment for Li^+ transport and charge transfer, allowing the modified cathode to sustain higher electrochemical utilization under fast cycling, especially when the kinetic limitations become much more severe at subzero temperatures.

As shown in Figure 2m,n, the long-term cycling results further confirm the superior electrochemical durability of NCM622@LBLS over a wide temperature range. At 25 °C, pristine NCM622 delivers an initial discharge capacity of 120.75 mAh g^{-1}, which rapidly decays to only 21.10 mAh g^{-1} after 500 cycles, corresponding to a capacity retention of merely 17.47%, whereas NCM622@LBLS exhibits a much higher initial capacity of 132.16 mAh g^{-1} and still maintains 109.5 mAh g^{-1} after 500 cycles, corresponding to a high retention of 82.85%. Notably, the final discharge capacity of NCM622@LBLS is about 5.19 times that of pristine NCM622, highlighting the remarkable role of the LBLS coating in suppressing capacity fading during prolonged cycling. A similarly improved cycling behavior is also observed at −20 °C, where the superiority of the LBLS coating becomes even more practically meaningful under harsh operating conditions. Pristine NCM622 only delivers an initial capacity of 85.47 mAh g^{-1} and retains 44.22 mAh g^{-1} after 500 cycles, corresponding to a capacity retention of 51.74%. In contrast, NCM622@LBLS starts from 126.02 mAh g^{-1}, and still maintains 101.57 mAh g^{-1} after 500 cycles, corresponding to a much higher retention of 80.60%. The final capacity of the coated sample is about 2.30 times that of bare NCM622, together with a higher average coulombic efficiency of 99.91% compared with 99.61% for pristine NCM622. The markedly improved cycling durability of NCM622@LBLS can be reasonably attributed to the synergistic effect of interfacial stabilization and structural preservation brought by the LBLS coating. The Li_2SO_4 and lithium borate-related surface species help build a more robust cathode–electrolyte interphase, which mitigates the accumulation of interfacial polarization, and alleviates the progressive degradation of the cathode surface during repeated cycling. At the same time, the well-preserved layered bulk structure ensures sustained structural integrity of the host material. As a result, NCM622@LBLS is able to maintain much higher reversible capacity and superior long-term cycling stability, especially under subzero conditions where interfacial instability and sluggish charge-transfer kinetics are greatly aggravated. These electrochemical results demonstrate the macroscopic performance benefits of LBLS modification; however, the structural origin of the improved cycling stability still needs to be clarified by directly tracking the lattice evolution of NCM622 during Li^+ extraction and insertion.

3.3. Structural Characterization and Kinetic Analysis

To further elucidate the effect of LBLS modification on the structural stability of NCM622 during electrochemical cycling, in situ XRD measurements were carried out to monitor the real time crystal structure evolution. As shown in Figure 3a,b, both pristine NCM622 and NCM622@LBLS exhibit the typical structural response of layered oxide cathodes, in which the diffraction peaks remain clearly identifiable throughout cycling, indicating that the layered framework is generally preserved. Among these reflections, the evolution of the (003) peak is particularly important because it is highly sensitive to the variation in interslab spacing along the c axis. The corresponding enlarged views of the (003) reflection during charge and discharge are further provided in Figures S13 and S14.

For pristine NCM622, the (003) peak shifts from 18.72° to 18.34° during charging and then returns to 18.61° upon discharge. In comparison, the (003) peak of NCM622@LBLS changes from 18.95° to 18.74° and finally recovers to 18.93°. Although both samples show the characteristic reversible movement of the (003) reflection during Li extraction and reinsertion, the extent of peak displacement is markedly different. The total peak shift in pristine NCM622 reaches 0.38°, whereas that of NCM622@LBLS is only 0.21°. In addition, the coated sample exhibits a much smaller deviation between the initial and recovered peak positions after discharge, indicating higher structural reversibility. These results suggest that the LBLS coating effectively moderates the lattice breathing behavior of NCM622 and

reduces the structural strain induced by Li^+ extraction/insertion. The lattice parameter evolution shown in Figure 3c,d further supports this conclusion. Along the a-axis, both samples show a gradual decrease during charging, which is associated with transition-metal oxidation and the contraction of TM–O bonds in the layered framework. However, the maximum shrinkage of the a-axis is reduced from 0.72% for pristine NCM622 to 0.51% for NCM622@LBLS, indicating that the in-plane lattice distortion is effectively alleviated after LBLS modification. A more pronounced difference is observed along the c-axis. During charging, the c-axis of pristine NCM622 undergoes a significant expansion with a Δc value of 2.10%, whereas the corresponding variation in NCM622@LBLS is reduced to 1.27%. This smaller c-axis fluctuation indicates that the LBLS-derived surface layer effectively moderates the anisotropic lattice breathing of the layered structure during delithiation. Since the c-axis evolution is closely related to the variation in interslab spacing and electrostatic interaction between adjacent oxygen layers, the reduced Δc value suggests that LBLS modification helps buffer the abrupt structural response of NCM622 at high states of charge and suppresses excessive lattice strain.

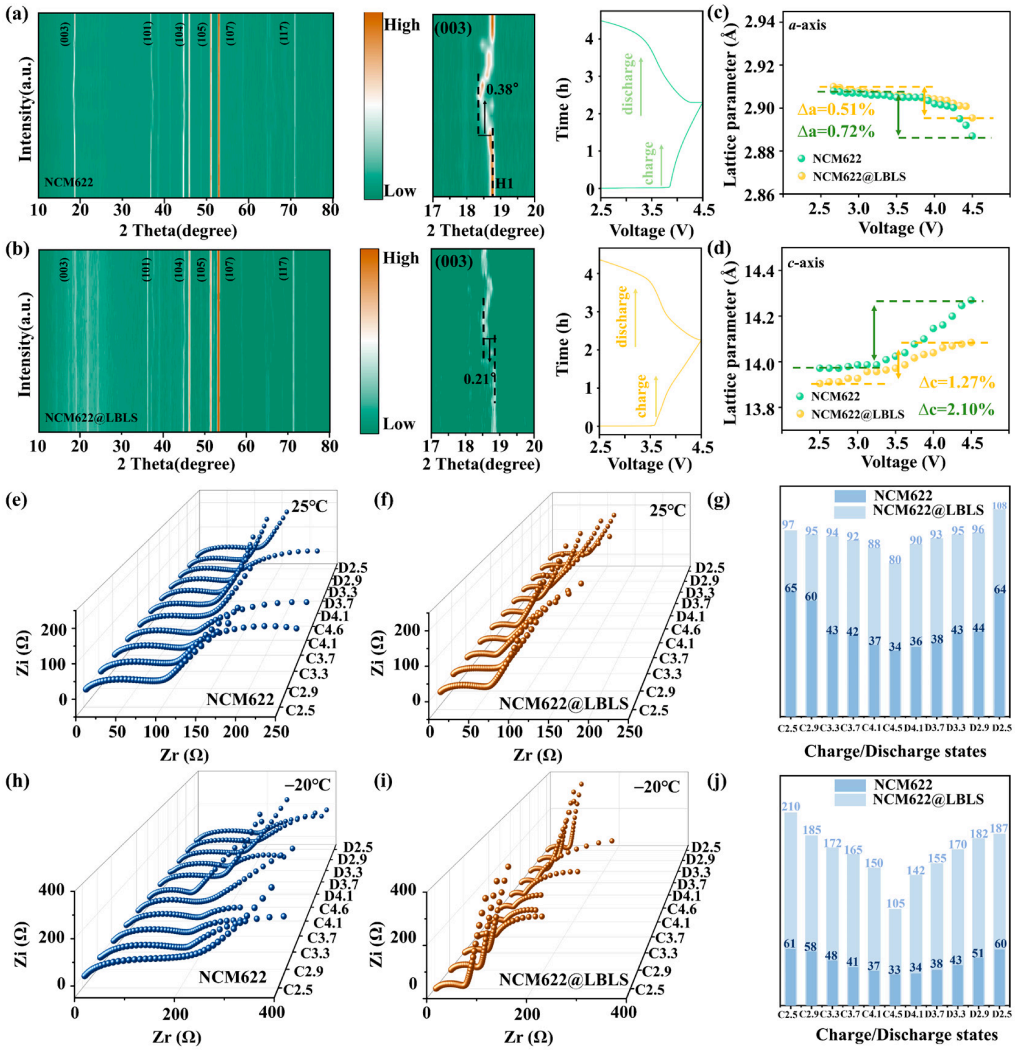


Figure 3. (**a**,**b**) In situ XRD contour plots collected during the first charge–discharge process at 0.1 C. Evolution of lattice parameters along the (**c**) a-axis and (**d**) c-axis during charging. (**e**,**f**) Nyquist plots of both pristine NCM622 and NCM622@LBLS cathodes recorded at 25 °C. (**g**) Comparison of R_{ct} values obtained from equivalent circuit fitting at 25 °C. (**h**,**i**) Nyquist plots recorded at −20 °C. (**j**) Comparison of R_{ct} values obtained from equivalent circuit fitting at −20 °C.

Overall, LBLS modification significantly enhances the structural reversibility of NCM622 during electrochemical cycling. The smaller (003) peak displacement, the better recovery of the peak position after discharge, and the reduced variations in both a- and c-axis lattice parameters collectively demonstrate that the coating effectively suppresses strain accumulation and mitigates phase-transition-induced structural fluctuation. This moderated lattice evolution helps relieve internal mechanical stress, reduce irreversible structural distortion, and preserve the crystallographic integrity of NCM622 during Li^+ extraction/insertion, thereby contributing to the improved cycling stability of NCM622@LBLS. In addition to the stabilized bulk lattice evolution, the interfacial charge-transfer behavior during different charge/discharge states was further examined, because low-temperature performance is also strongly governed by the evolution of electrode/electrolyte interfacial resistance.

To further correlate the improved structural reversibility with electrochemical interfacial kinetics, ex situ EIS measurements were carried out at different charge/discharge states at 25 °C and −20 °C. As shown in Figure 3e,f, the Nyquist plots collected at 25 °C exhibit state-of-charge-dependent semicircles for both pristine NCM622 and NCM622@LBLS, reflecting the dynamic evolution of interfacial charge-transfer resistance during Li^+ extraction/insertion. The fitted resistance values are summarized in Figure 3g. For pristine NCM622, the resistance decreases from 97 Ω at C2.5 to 80 Ω at C4.5 during charging, and then increases again from 90 Ω at D4.1 to 108 Ω at D2.5 during discharge. This variation indicates that the interfacial kinetics of NCM622 are strongly affected by the charge/discharge state, and the resistance becomes more pronounced again after relithiation. In comparison, NCM622@LBLS shows much lower resistance values over the entire process, decreasing from 65 Ω at C2.5 to 34 Ω at C4.5 during charging and then increasing moderately from 36 Ω at D4.1 to 64 Ω at D2.5 during discharge. The consistently lower resistance of NCM622@LBLS demonstrates that the LBLS coating effectively reduces the interfacial charge-transfer barrier and maintains faster reaction kinetics at room temperature. This kinetic advantage becomes more significant under low-temperature conditions. As shown in Figure 3h,i, the semicircles of pristine NCM622 become much larger at −20 °C, indicating severely sluggish charge transfer and intensified interfacial polarization. The fitted resistance values in Figure 3j further confirm this behavior. For pristine NCM622, the resistance remains at a high level throughout the charge/discharge process, decreasing from 210 Ω at C2.5 to 105 Ω at C4.5 during charging and increasing again to 187 Ω at D2.5 during discharge. Such large resistance values reveal that the pristine cathode suffers from serious kinetic limitation at subzero temperature. In sharp contrast, NCM622@LBLS exhibits remarkably lower resistance values of 61, 58, 48, 41, 37, and 33 Ω from C2.5 to C4.5, and 34, 38, 43, 51, and 60 Ω during the subsequent discharge process. Compared with pristine NCM622, NCM622@LBLS exhibits significantly reduced resistance values throughout the charge/discharge process at −20 °C, demonstrating that the LBLS coating effectively suppresses low-temperature interfacial polarization.

In total, the lower resistance and more favorable interfacial kinetics of NCM622@LBLS can be attributed to the interfacial regulation induced by the LBLS coating. At 25 °C, the LBLS-derived surface layer reduces the direct contact between the reactive NCM622 surface and the electrolyte, thereby suppressing continuous parasitic reactions and decreasing the charge-transfer barrier during Li^+ extraction/insertion. As a result, NCM622@LBLS maintains lower resistance values than pristine NCM622 over the whole charge/discharge process. At −20 °C, the sluggish interfacial Li^+ transport, increased electrolyte viscosity, and aggravated polarization normally lead to a sharp increase in charge-transfer resistance. Under such kinetically unfavorable conditions, the protective effect of the LBLS coating becomes more significant. The lithium borate/sulfate-containing surface layer

stabilizes the cathode/electrolyte interface, mitigates the accumulation of resistive decomposition products, and facilitates more stable interfacial charge transfer. Consequently, NCM622@LBLS exhibits much lower and more stable resistance values throughout the charge/discharge process at both 25 °C and −20 °C, demonstrating that LBLS modification effectively improves the interfacial reaction kinetics, especially under low-temperature conditions. Although the ex situ EIS results confirm the reduced interfacial resistance of NCM622@LBLS, a more detailed kinetic analysis is still required to distinguish the individual relaxation processes and Li^+ diffusion behavior responsible for the enhanced low-temperature electrochemical response.

To gain deeper insight into the kinetic origin of the improved electrochemical behavior, distribution of relaxation times analysis and galvanostatic intermittent titration measurements were further carried out at 25 °C and −20 °C. At 25 °C, NCM622@LBLS exhibits lower $\gamma(\tau)$ intensities than pristine NCM622 over almost the entire characteristic-time range (Figure 4a–h), with particularly obvious decreases in the τ2–τ4 regions and an additional weakening of the τ5 response. This result indicates that LBLS modification suppresses polarization over the full kinetic sequence from the interface to the bulk. Specifically, the reduced τ1 contribution suggests that the rapid interfacial resistance is alleviated and Li^+ migration through the surface region becomes more facile. The suppressed τ2 and τ3 responses indicate a reduced charge-transfer barrier and a slower accumulation of interfacial overpotential during the electrochemical reaction. Meanwhile, the weakened τ4 and τ5 features imply that the slow relaxation behavior related to solid-state diffusion and concentration equilibration is also mitigated, meaning that the lithiation and delithiation process can proceed in a more homogeneous manner with less severe concentration polarization. Therefore, at room temperature, the LBLS coating not only improves the fast interfacial kinetics but also reduces the delayed bulk relaxation processes that usually emerge during sustained electrochemical operation. At −20 °C, the DRT evolution becomes more differentiated (Figure 4i–p). The τ1–τ3 responses of NCM622@LBLS remain clearly lower than those of pristine NCM622, especially in the τ3 region, indicating that the LBLS layer still effectively relieves the fast and intermediate kinetic polarization under subzero conditions. Such lower intensities suggest the coated electrode can reduce the early-stage interfacial bottleneck, suppress the rapid buildup of polarization, and maintain a more prompt electrochemical response during charge transfer. However, unlike the behavior at 25 °C, the τ4 and τ5 intensities of NCM622@LBLS become higher than those of pristine NCM622 at −20 °C. This distinct change suggests that the rate-limiting processes are redistributed after surface modification. For pristine NCM622, the electrochemical reaction at −20 °C is more severely hindered in the surface and interfacial region, so the reaction cannot effectively propagate into the particle interior, and the slow bulk-related relaxation processes are not fully developed. After LBLS coating, the short-time interfacial bottlenecks are alleviated, allowing the electrochemical reaction to involve a larger fraction of the active material. As a result, the remaining low-temperature limitation becomes increasingly governed by slower bulk diffusion, concentration equilibration, and structural accommodation, which makes the τ4 and τ5 responses more pronounced. This behavior indicates a shift in the dominant kinetic limitation from short-time interfacial processes toward slower bulk-related relaxation, reflecting deeper electrochemical participation of the active material rather than a simple deterioration of the overall kinetic behavior.

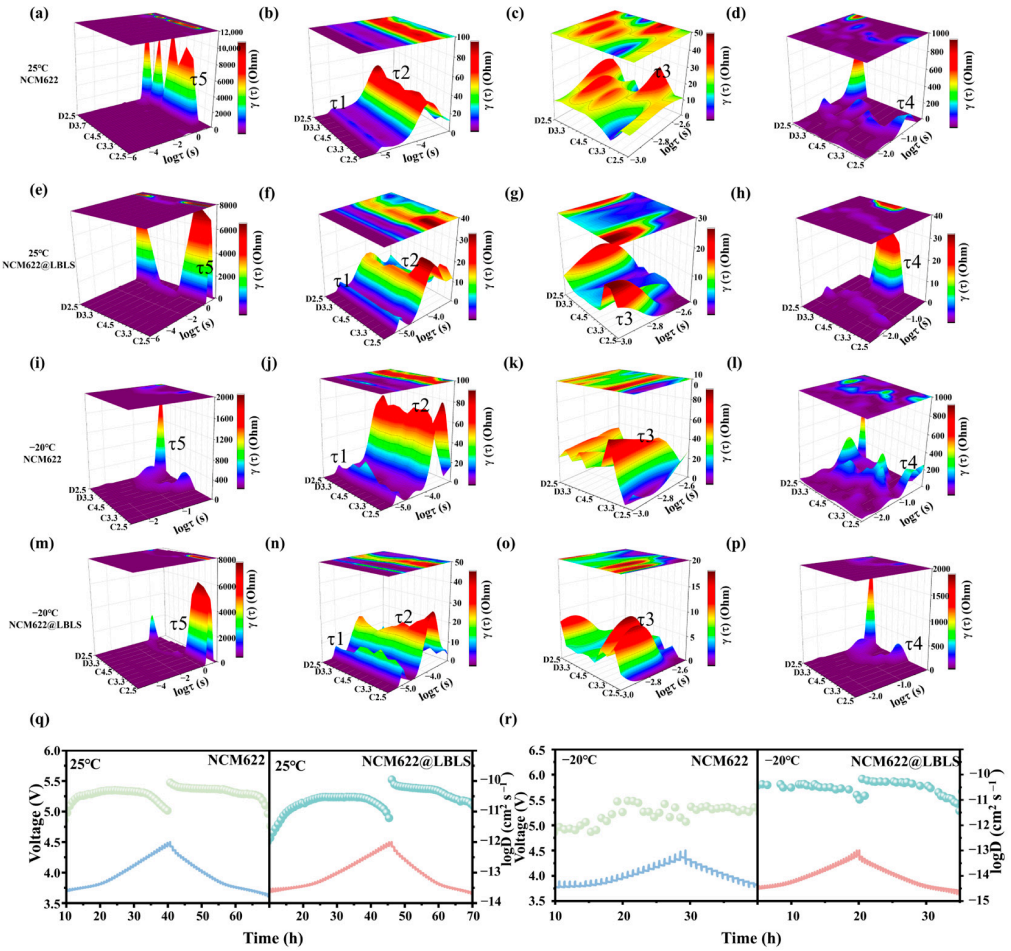


Figure 4. (**a**–**d**) DRT spectra of pristine NCM622 during dynamic charge/discharge processes at 25 °C. (**e**–**h**) DRT spectra of NCM622@LBLS at 25 °C. (**i**–**l**) DRT spectra of pristine NCM622 at −20 °C. (**m**–**p**) DRT spectra of NCM622@LBLS at −20 °C. (**q**,**r**) GITT-derived Li^+ diffusion coefficients (D_{Li+}) at (**q**) 25 °C and (**r**) −20 °C.

The GITT results provide further evidence for the effect of LBLS modification on Li^+ diffusion kinetics (Figure 4q,r). At 25 °C, both pristine NCM622 and NCM622@LBLS exhibit Li^+ diffusion coefficients mainly on the order of 10^{-11} to 10^{-10} cm^2 s^{-1} throughout the charge and discharge process. Compared with pristine NCM622, NCM622@LBLS shows only a slightly higher behavior at room temperature, suggesting that the coating can moderately facilitate Li^+ migration and improve the stability of the diffusion process under relatively mild kinetic conditions. A much more pronounced difference is observed at −20 °C. For pristine NCM622, the apparent Li^+ diffusion coefficients decrease markedly and are mainly distributed in the range of about 10^{-12} to 10^{-11} cm^2 s^{-1}, indicating severely hindered Li^+ transport under subzero conditions. In contrast, NCM622@LBLS still maintains diffusion coefficients largely in the range of about 10^{-11} to 10^{-10} cm^2 s^{-1} over most of the tested process. In other words, after LBLS coating, the Li^+ diffusion kinetics at low temperature are improved by roughly one order of magnitude within a broad state-of-charge region. Such a clear enhancement indicates that the LBLS-derived surface layer can effectively alleviate the sluggish Li^+ transport behavior that usually dominates at low temperature. Li^+ can migrate more efficiently across the electrode/electrolyte interface and further penetrate into the layered bulk, thereby reducing concentration polarization and helping the reaction proceed more uniformly throughout the particle. As a result, the cathode can sustain deeper lithiation and delithiation even under subzero conditions,

which is beneficial for improving active-material utilization and suppressing the rapid kinetic deterioration commonly encountered at low temperature.

To further clarify the chemical origin of the improved low-temperature interfacial stability, depth-profiling XPS was performed on pristine NCM622 and NCM622@LBLS cathodes after 100 cycles at −20 °C. The spectra collected after sputtering for 0, 80, and 160 s reveal the chemical evolution from the outer surface to the inner region of the cathode/electrolyte interphase. Because low-temperature operation strongly amplifies interfacial polarization and charge-transfer resistance, the depth-dependent CEI chemistry provides direct evidence for evaluating the protective function of the LBLS coating. In the C 1s spectra of pristine NCM622, the fitted peaks at 284.79, 285.85, 286.52, 288.71, and 290.64 eV at 0 s are assigned to C–C, C–H, C–O, C=O, and O–C=O species, respectively (Figure 5a). After sputtering for 80 s, these peaks are located at 284.75, 285.65, 286.90, 288.70, and 290.50 eV, and they further appear at 284.75, 285.70, 287.00, 288.65, and 290.40 eV after sputtering for 160 s. These small binding-energy variations demonstrate that the main carbon-containing species remain similar along the depth direction. However, their relative contents change markedly. At the outermost surface, the C–O, C=O, and O–C=O components account for 22.6%, 7.2%, and 22.9%, respectively, giving a total oxygenated carbon fraction of 52.7%, as quantified in Figure S15. These oxygenated carbon species are assigned to carbonate-electrolyte decomposition products, including lithium alkyl carbonates, lithium carbonate, and polymerized organic carbonates. After sputtering for 80 and 160 s, the total oxygenated carbon fractions decrease to 26.5% and 28.7%, respectively. This depth evolution demonstrates that pristine NCM622 forms a CEI with severe outer-surface accumulation of carbonate-derived decomposition products after low-temperature cycling. For NCM622@LBLS, the C 1s peaks at 0 s are located at 284.78, 285.59, 286.38, 288.73, and 290.40 eV, corresponding to C–C, C–H, C–O, C=O, and O–C=O species, respectively (Figure 5e). After sputtering for 80 s, the corresponding peaks appear at 284.72, 285.77, 287.06, 288.86, and 290.90 eV, and after 160 s they are located at 284.70, 285.54, 286.59, 288.34, and 290.89 eV. Compared with pristine NCM622, no obvious systematic peak shift is observed, indicating that LBLS modification does not change the basic types of carbon-containing species formed after cycling. The major difference lies in the relative distribution. At 0 s, the C–O, C=O, and O–C=O fractions of NCM622@LBLS are 14.4%, 8.7%, and 12.4%, respectively, giving a total oxygenated carbon fraction of 35.5%, much lower than the 52.7% of pristine NCM622 (Figure S16). In particular, the O–C=O contribution decreases from 22.9% to 12.4%, confirming that the LBLS coating suppresses the excessive accumulation of carbonate-derived decomposition products on the outer cathode surface. After sputtering for 80 and 160 s, the oxygenated carbon fractions are 29.0% and 34.9%, respectively, indicating that electrolyte decomposition products still exist within the interphase but are not strongly concentrated on the outermost surface. Therefore, the LBLS coating regulates the spatial distribution of carbonaceous CEI species and alleviates the formation of a thick organic-rich surface layer.

The Li 1s spectra further distinguish the lithium-containing interfacial species (Figure 5b,f). For pristine NCM622, the Li–O and Li–F components are located at 55.55 and 56.20 eV at 0 s, respectively. Their peak positions remain unchanged after sputtering for 80 and 160 s, with Li–O at 55.55 eV and Li–F at 56.20 eV. This stable peak position indicates that similar Li-containing species are distributed throughout the CEI. In terms of relative content, the Li–F fraction increases from 42.5% at 0 s to 52.9% and 56.9% at 80 and 160 s, while the Li–O fraction decreases from 57.5% to 47.1% and 43.1%, respectively, as shown in Figure S17. This trend confirms that LiF-containing salt-decomposition products are present in the inner CEI of pristine NCM622. However, these LiF species coexist with abundant carbonate-derived organic products, as demonstrated by the high oxygenated

carbon content in the C 1s spectra. Therefore, the pristine CEI is not a compact inorganic protective layer, but a mixed interphase containing both LiF and extensive organic decomposition products. For NCM622@LBLS, the Li–O component is located at 55.49, 55.55, and 55.55 eV after sputtering for 0, 80, and 160 s, respectively, while the Li–F component shifts from 56.27 eV at 0 s to 56.41 and 56.45 eV at 80 and 160 s (Figure 5f). More importantly, the Li–O contribution of NCM622@LBLS remains higher than that of pristine NCM622 at all sputtering depths, accounting for 62.7%, 54.5%, and 48.9% at 0, 80, and 160 s, respectively, while the corresponding Li–F fractions are 37.3%, 45.5%, and 51.1% (Figure S18). Therefore, the enhanced interface of NCM622@LBLS should not be described as simply LiF-rich. Instead, the higher and more persistent Li–O signal confirms the participation of LBLS-derived Li–O-containing inorganic species, including Li_2O-, lithium borate-, and lithium sulfate-related components. These species participate in building a composite inorganic interphase and contribute to a more stable cathode/electrolyte interface.

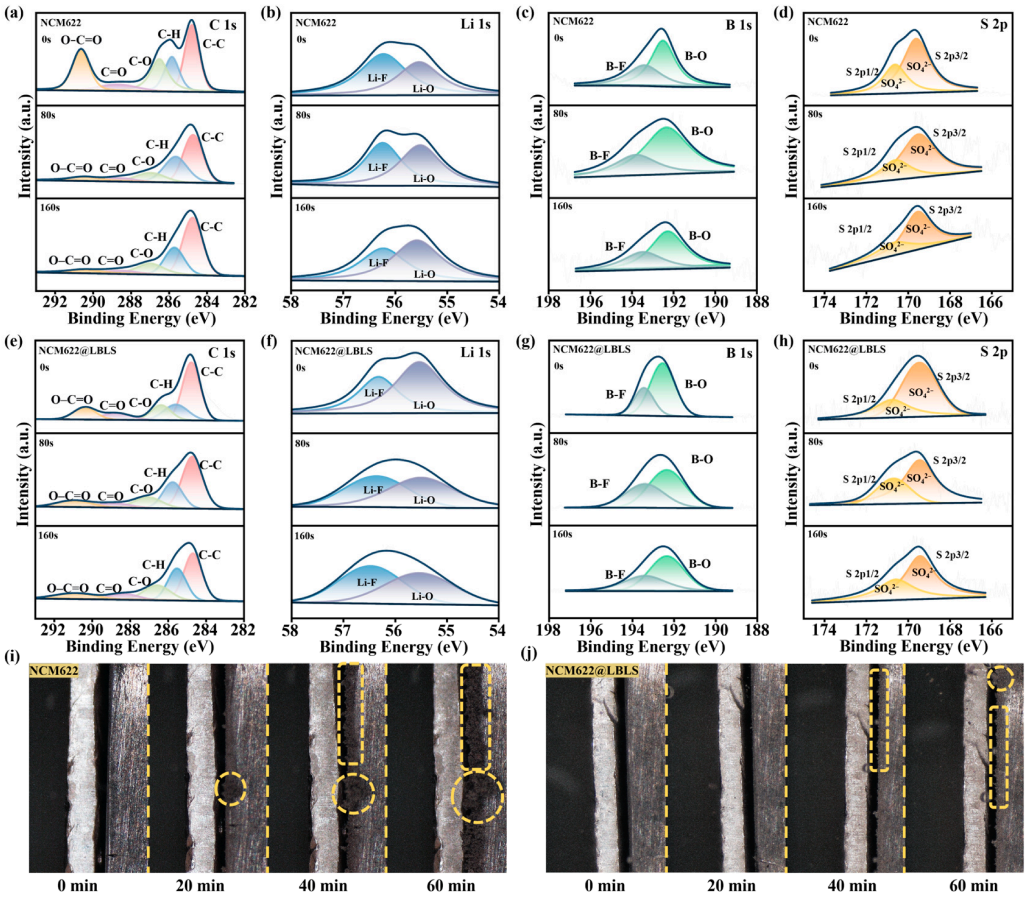


Figure 5. (**a**–**d**) Depth-profiling XPS spectra of NCM622 after 100 cycles at −20 °C: (**a**) C 1s, (**b**) Li 1s, (**c**) B 1s and (**d**) S 2p. (**e**–**h**) Depth-profiling XPS spectra of NCM622@LBLS after 100 cycles at −20 °C: (**e**) C 1s, (**f**) Li 1s, (**g**) B 1s and (**h**) S 2p. (**i**,**j**) In situ observation of lithium dendrite evolution on the lithium anode surface during cycling.

The B 1s spectra provide direct evidence for the borate-related interfacial framework (Figure 5c,g). For pristine NCM622, the B–O and B–F components are located at 192.50 and 193.40 eV at 0 s, respectively. After sputtering for 80 s, the B–O and B–F peaks shift to 192.30 and 193.80 eV, and after 160 s they appear at 192.20 and 193.50 eV. These B–O and B–F species are assigned to borate and fluoroborate products generated from the decomposition of boron-containing electrolyte salts, including $LiBF_4$ and LiDFOB. The B–O fraction is 61.5%, 70.8%, and 64.8% at 0, 80, and 160 s, respectively. However, the total B 1s peak area decreases sharply at 0 s to 80 and 160 s (Figure S19). This result demonstrates

that the B-containing products in pristine NCM622 mainly originate from electrolyte-salt decomposition and are not retained as a stable boron-containing framework in the inner interphase. In contrast, NCM622@LBLS exhibits a stronger and more depth-retained B 1s signal. The B–O component is located at 192.55 eV at 0 s and remains at 192.35 eV after sputtering for both 80 and 160 s, while the B–F component appears at 193.30, 193.40, and 193.40 eV, respectively (Figure 5g). The B–O component accounts for 70.0%, 58.5%, and 61.9% at 0, 80, and 160 s, confirming that B–O species remain the dominant boron-containing component throughout the interphase. More importantly, the total B 1s peak area of NCM622@LBLS is much higher than that of pristine NCM622, especially after 160 s sputtering; this stronger depth-retained B signal is shown in Figure S20. These results confirm that the LBLS coating introduces a stable borate-related inorganic framework into the cathode interphase. The coexistence of B–O and B–F species demonstrates that the cycled CEI is constructed by both the pre-existing LBLS layer and boron-containing electrolyte-salt decomposition. This boron-containing inorganic network enhances the chemical robustness and spatial continuity of the CEI, thereby suppressing uncontrolled electrolyte decomposition on the cathode surface.

The S 2p spectra further reveal the different sulfur-containing interfacial chemistry (Figure 5d,h). For pristine NCM622, the S $2p_{3/2}$ and S $2p_{1/2}$ peaks are located at 169.60 and 170.60 eV at 0 s, respectively. After sputtering for 80 s, they appear at 169.50 and 170.60 eV, and after 160 s they are located at 169.50 and 170.68 eV. These peaks are assigned to SO_4^{2-}-type oxidized sulfur species generated from LiFSI decomposition during low-temperature cycling. The S $2p_{3/2}$ component accounts for 68.1%, 72.1%, and 67.6% at 0, 80, and 160 s, while the S $2p_{1/2}$ component contributes 31.9%, 27.9%, and 32.4%, respectively. Although the spin–orbit doublet remains stable in position, the total S 2p peak area decreases dramatically from 0 s to 80 and 160 s (Figure S21). This result confirms that LiFSI-derived sulfur-containing decomposition products are mainly accumulated on the outer surface of pristine NCM622. Together with the high outer-surface oxygenated carbon fraction, the surface-enriched SO_4^{2-} species demonstrate severe salt/solvent decomposition and the formation of a poorly regulated CEI on pristine NCM622. For NCM622@LBLS, the S $2p_{3/2}$ and S $2p_{1/2}$ peaks are located at 169.46 and 170.70 eV at 0 s, 169.45 and 170.70 eV at 80 s, and 169.48 and 170.64 eV at 160 s, respectively (Figure 5h). The S $2p_{3/2}$ fraction is 67.1%, 70.9%, and 63.8% at 0, 80, and 160 s, while the corresponding S $2p_{1/2}$ fraction is 32.9%, 29.1%, and 36.2%. Unlike pristine NCM622, the total S 2p peak area of NCM622@LBLS changes from 0 s to 80 and 160 s, indicating stronger sulfur retention within the interphase. Figure S22 further illustrates this depth-retained distribution. Although the outermost S signal is much weaker than that of pristine NCM622, the sulfur-containing signal is better retained after sputtering. Since the LBLS coating contains Li_2SO_4-related components, these SO_4^{2-}-type species are attributed to the coating-derived sulfate framework together with LiFSI-derived interfacial products. The stronger retention of the sulfur signal after sputtering indicates a different depth distribution of sulfur-containing species in NCM622@LBLS.

Overall, the depth-profiling XPS results demonstrate that LBLS modification reconstructs the low-temperature CEI chemistry from a surface-accumulated decomposition layer into a composite inorganic-reinforced interphase. These results show that B–O-containing species are more strongly retained through the depth of the CEI in NCM622@LBLS than in pristine NCM622. Such a chemically regulated CEI suppresses excessive electrolyte decomposition, stabilizes the cathode/electrolyte interface, and supports more stable charge-transfer behavior during low-temperature cycling, thereby explaining the lower interfacial resistance, improved kinetic response, and enhanced low-temperature cycling stability of NCM622@LBLS. Since the stability of the cathode interface can also influence Li^+ flux distribution and deposition behavior on the Li metal anode in half cells, in situ

optical microscopy was further used to evaluate whether the LBLS-modified cathode contributes to more uniform Li deposition. The CEI formed on NCM622@LBLS contains a greater relative contribution from Li-O, B-O/B-F, and sulfate-related species and a lower contribution from oxygenated carbon products. Such tailored interfacial composition slows continuous cathode–electrolyte degradation and reduces charge transfer impedance, providing solid chemical evidence for the declined interfacial polarization of NCM622@LBLS. This compositional difference is consistent with the reduced interfacial resistance observed electrochemically.

In situ optical microscopy was further employed to visualize the Li deposition behavior on the Li metal anode during cycling (Figure 5i,j). In the cell paired with pristine NCM622, the Li metal surface gradually becomes uneven as the deposition time increases. At 20 min, localized protrusions begin to appear at the Li/electrolyte interface. After 40 and 60 min, more obvious dendritic and mossy Li deposits can be observed, indicating nonuniform Li deposition and aggravated interfacial instability. In contrast, the Li metal anode paired with NCM622@LBLS exhibits a much more stable deposition morphology. During the same observation period, only limited local fluctuations are observed, and the growth of dendritic Li is markedly suppressed. This difference indicates that the NCM622@LBLS-based cell enables a more homogeneous Li^+ flux and a more uniform local current-density distribution at the Li metal surface. For the pristine NCM622 system, continuous interfacial side reactions and accumulated polarization promote uneven Li nucleation, causing Li to preferentially deposit at local protrusions and further evolve into dendritic or mossy structures. After LBLS modification, the overall interfacial reaction becomes more stable, which reduces polarization-induced Li^+ flux inhomogeneity and guides more uniform Li deposition. Therefore, the suppressed dendrite growth in the NCM622@LBLS system further confirms its improved interfacial stability and contributes to safer and more durable low-temperature cycling.

4. Conclusions

In summary, we developed a multifunctional Li_2O-B_2O_3-Li_2SO_4 composite coating on NCM622 through a simple wet-mixing/calcination strategy to improve its low-temperature electrochemical performance. Different from a conventional inert protective layer, the LBLS coating acts as an interfacial regulator that simultaneously stabilizes surface chemistry, promotes Li^+ transport, and buffers structural fluctuation during Li^+ extraction/insertion. Structural and surface characterizations confirm that the LBLS-derived layer is successfully constructed on the particle surface without destroying the layered α-$NaFeO_2$ framework of NCM622. The appearance of B–O and sulfate-related species, together with the continuous surface-modified layer observed by SEM, STEM-EDS and TEM, verifies the effective introduction of Li_2O-B_2O_3-Li_2SO_4-derived components. Benefiting from this surface regulation, NCM622@LBLS exhibits significantly improved electrochemical performance over a wide temperature range. At 25 °C, the charge-transfer resistance decreases from 104 Ω for pristine NCM622 to 70 Ω after LBLS modification. When the temperature is lowered to −20 °C, NCM622@LBLS still maintains a lower resistance of 110 Ω, compared with 160 Ω for pristine NCM622, demonstrating its ability to suppress low-temperature interfacial polarization. More importantly, after 500 cycles at −20 °C, NCM622@LBLS maintains 101.57 mAh g^{-1} with a capacity retention of 80.60%, much higher than the 44.22 mAh g^{-1} and 51.74% retention of pristine NCM622. This improvement confirms the effectiveness of LBLS coating in enhancing low-temperature cycling durability. The underlying enhancement arises from the combined optimization of lattice stability, interfacial kinetics and CEI chemistry. In situ XRD reveals that LBLS modification reduces the total (003) peak shift from 0.38° to 0.21°, and decreases the a-axis and c-axis variations from 0.72% and 2.10%

to 0.51% and 1.27%, respectively, indicating suppressed anisotropic lattice breathing. Ex situ EIS and DRT analyses further show lower interfacial resistance and weaker kinetic polarization at different charge/discharge states, while GITT confirms faster Li^+ diffusion at −20 °C. Depth-profiling XPS demonstrates that LBLS suppresses carbonate-derived decomposition products and promotes the formation of an inorganic-reinforced CEI containing Li–O, B–O/B–F and SO_4^{2-}-type species. In situ optical microscopy further verifies more uniform Li deposition and suppressed dendrite growth in cells paired with NCM622@LBLS. This work therefore provides a practical surface-engineering strategy for addressing the coupled kinetic, interfacial and structural degradation of layered oxide cathodes under low-temperature conditions.

Supplementary Materials: The following supporting information can be downloaded at: https://www.mdpi.com/article/10.3390/met16080830/s1, Figure S1: Long-term cycling performance of NCM622 coated with 1 wt%, 3 wt% and 5 wt% LBLS over 100 cycles at −20°C; Figure S2: Enlarged XRD pattern of NCM622 and NCM622@LBLS; Figure S3: XPS survey spectra of pristine NCM622 and NCM622@LBLS; Figure S4: XPS spectra of O 1s for pristine NCM622 and NCM622@LBLS; Figure S5: SEM images of pristine NCM622 and NCM622@LBLS; Figure S6: FFT patterns corresponding to regions I and II in Figure 1k,m; Figure S7: Inverse FFT images corresponding to regions I and II in Figure 1k,m; Figure S8: The HRTEM image of NCM622@3 wt% LBLS; Figure S9: Fitted charge-transfer resistance values of pristine NCM622 and NCM622@LBLS at 25 °C; Figure S10: Fitted charge-transfer resistance values of pristine NCM622 and NCM622@LBLS at −20 °C; Figure S11: Linear relationships between log(i) and log(v) for pristine NCM622 and NCM622@LBLS at 25 °C. The b values were obtained by fitting the corresponding CV peak currents; Figure S12: Capacitive contribution ratios of pristine NCM622 and NCM622@LBLS at different scan rates at 25 °C; Figure S13: In situ XRD evolution of pristine NCM622 during charge and discharge; Figure S14: In situ XRD evolution of NCM622@LBLS during charge and discharge; Figure S15: Normalized relative contents of representative chemical bonds of pristine NCM622 as a function of sputtering time: C 1s; Figure S16: Normalized relative contents of representative chemical bonds of NCM622@LBLS as a function of sputtering time: C 1s; Figure S17: Normalized relative contents of representative chemical bonds of pristine NCM622 as a function of sputtering time: Li 1s; Figure S18: Normalized relative contents of representative chemical bonds of NCM622@LBLS as a function of sputtering time: Li 1s; Figure S19: Normalized relative contents of representative chemical bonds of pristine NCM622 as a function of sputtering time: B 1s; Figure S20: Normalized relative contents of representative chemical bonds of NCM622@LBLS as a function of sputtering time: B 1s; Figure S21: Normalized relative contents of representative chemical bonds of pristine NCM622 as a function of sputtering time: S 2p; Figure S22: Normalized relative contents of representative chemical bonds of NCM622@LBLS as a function of sputtering time: S 2p; Table S1: Electrochemical comparison of surface-modified NCM622 cathodes.

Author Contributions: Conceptualization, Y.S.; methodology, Y.S.; formal analysis, X.L., Z.L. and H.B.; investigation, E.C. and M.S.; resources, Y.S.; data curation, Z.L., H.B., Z.Z., M.S., X.G. and M.Z.; writing—original draft preparation, Y.S.; writing—review and editing, Z.L., E.C. and X.G.; visualization, X.L., H.B., Z.Z. and M.S.; supervision, Y.S. and M.Z.; project administration, Y.S.; funding acquisition, Y.S.; validation, X.L., Z.Z., X.G. and M.Z. writing—original draft preparation, B.Z.; methodology, S.P. and Q.Y.; formal analysis, B.Z. and V.B.; investigation, B.X.; data curation, Q.Y. and V.B.; writing—review and editing, (none); visualization, B.X.; supervision, Q.Y.; validation, B.Z., S.P. and B.X. All authors have read and agreed to the published version of the manuscript.

Funding: This work was financially supported by the National Key R&D Program of China (2024YFE0108500), the Jiangsu Province Qinglan Project.

Data Availability Statement: The original contributions presented in this study are included in the article/Supplementary Materials. Further inquiries can be directed to the corresponding authors.

Conflicts of Interest: The authors declare no conflict of interest.

References

1. Li, M.; Lu, J.; Chen, Z.; Amine, K. 30 Years of Lithium-Ion Batteries. *Adv. Mater.* **2018**, *30*, 1800561. [CrossRef] [PubMed]
2. Li, F.; Mo, F.; Zhong, C.; Chen, Y.; Liu, Z.; Duan, Y.; Ma, X.; Fan, Y.; Dong, X.; Chen, Z.; et al. A Roadmap toward High-Performance Hard Carbon for Sodium-Ion Batteries: From Fundamental Studies on Synthesis and Mechanism to Practical Application. *Energy Storage Mater.* **2025**, *83*, 104668. [CrossRef]
3. Ngoy, K.R.; Lukong, V.T.; Yoro, K.O.; Makambo, J.B.; Chukwuati, N.C.; Ibegbulam, C.; Eterigho-Ikelegbe, O.; Ukoba, K.; Jen, T.-C. Lithium-Ion Batteries and the Future of Sustainable Energy: A Comprehensive Review. *Renew. Sustain. Energy Rev.* **2025**, *223*, 115971. [CrossRef]
4. Chen, S.; Wei, X.; Zhang, G.; Wang, X.; Zhu, J.; Feng, X.; Dai, H.; Ouyang, M. All-Temperature Area Battery Application Mechanism, Performance, and Strategies. *Innovation* **2023**, *4*, 100465. [CrossRef] [PubMed]
5. Meng, F.; Xiong, X.; Tan, L.; Yuan, B.; Hu, R. Strategies for Improving Electrochemical Reaction Kinetics of Cathode Materials for Subzero-Temperature Li-Ion Batteries: A Review. *Energy Storage Mater.* **2022**, *44*, 390–407. [CrossRef]
6. Piao, N.; Gao, X.; Yang, H.; Guo, Z.; Hu, G.; Cheng, H.-M.; Li, F. Challenges and Development of Lithium-Ion Batteries for Low Temperature Environments. *eTransportation* **2022**, *11*, 100145. [CrossRef]
7. Zhang, N.; Deng, T.; Zhang, S.; Wang, C.; Chen, L.; Wang, C.; Fan, X. Critical Review on Low-Temperature Li-Ion/Metal Batteries. *Adv. Mater.* **2022**, *34*, 2107899. [CrossRef] [PubMed]
8. Luo, L.; Chen, K.; Chen, H.; Li, H.; Cao, R.; Feng, X.; Chen, W.; Fang, Y.; Cao, Y. Enabling Ultralow-Temperature (−70 °C) Lithium-Ion Batteries: Advanced Electrolytes Utilizing Weak-Solvation and Low-Viscosity Nitrile Cosolvent. *Adv. Mater.* **2024**, *36*, 2308881. [CrossRef] [PubMed]
9. Chen, W.; Zhang, H.; Zhang, D.; Muhtar, D.; Li, K.; Shi, Y.; Lu, X.; Sun, Y.; Zou, L.; Lu, X. Practical Multiphase Transition Kinetics in High-Energy-Density Layered Cathodes. *J. Am. Chem. Soc.* **2026**, *148*, 13744–13754. [CrossRef] [PubMed]
10. Shen, Y.; Xue, H.; Wang, S.; Zhang, D.; Yin, D.; Wang, L.; Cheng, Y. Ammonia-Low Coprecipitation Synthesis of Lithium Layered Oxide Cathode Material for High-Performance Battery. *Chem. Eng. J.* **2021**, *411*, 128487. [CrossRef]
11. Hou, J.; Yang, M.; Wang, D.; Zhang, J. Fundamentals and Challenges of Lithium Ion Batteries at Temperatures between −40 and 60 °C. *Adv. Energy Mater.* **2020**, *10*, 1904152. [CrossRef]
12. Meng, X.-H.; Xiao, D.; Zhou, Z.-Y.; Liu, W.-Z.; Shi, J.-L.; Wan, L.-J.; Guo, Y.-G. Self-Limiting Phase Transition Enabling Reversible Overstoichiometric Li Storage in Ni-Rich Cathodes. *J. Am. Chem. Soc.* **2024**, *146*, 14889–14897. [CrossRef] [PubMed]
13. Hu, Q.; Wu, Y.; Ren, D.; Liao, J.; Song, Y.; Liang, H.; Wang, A.; He, Y.; Wang, L.; Chen, Z.; et al. Revisiting the Initial Irreversible Capacity Loss of $LiNi_{0}.6Co_{0.2}Mn_{0.2}O_2$ Cathode Material Batteries. *Energy Storage Mater.* **2022**, *50*, 373–379. [CrossRef]
14. Du, K.; Gao, A.; Gao, L.; Sun, S.; Lu, X.; Yu, C.; Li, S.; Zhao, H.; Bai, Y. Enhancing the Structure Stability of Ni-Rich $LiNi_{0.6}Co_{0.2}Mn_{0.2}O_2$ Cathode via Encapsulating in Negative Thermal Expansion Nanocrystalline Shell. *Nano Energy* **2021**, *83*, 105775. [CrossRef]
15. Zhou, H.; Hou, W.; Zhu, D.; Zhou, P.; Peng, X.; Liu, Z.; Yan, S.; Lu, Y.; Ou, Y.; Liu, F.; et al. Controlled Anodic Decomposition Pathway of Supramolecular Lithium Borate for Rationally Tuned Interphase Chemistry. *Angew. Chem. Int. Ed.* **2025**, *64*, e202500425. [CrossRef] [PubMed]
16. Liu, Y.; Xin, Y.; He, B.; Zhang, F.; Wang, C.; Tian, H. High Entropy Fine-Tuning Achieves Fast Li^+ Kinetics in High-Performance Co-Free High-Ni Layered Cathodes. *Adv. Mater.* **2025**, *37*, 2417353. [CrossRef] [PubMed]
17. Xu, M.; Lu, J.; Sun, Z.; Yang, M.; Sheng, B.; Chen, M.; Chen, J.; Zhang, Q.; Han, X. Lanthanum Doping and Surface Li_3BO_3 Passivating Layer Enabling 4.8 V Nickel-Rich Layered Oxide Cathodes toward High Energy Lithium-Ion Batteries. *J. Colloid Interface Sci.* **2024**, *673*, 386–394. [CrossRef] [PubMed]
18. He, H.; Wang, L.; Al-Abbasi, M.; Cao, C.; Li, H.; Xu, Z.; Chen, S.; Zhang, W.; Li, R.; Lai, Y.; et al. Interface Engineering on Constructing Physical and Chemical Stable SOLID-STATE Electrolyte toward Practical Lithium Batteries. *Energy Environ. Mater.* **2024**, *7*, e12699. [CrossRef]
19. Liang, L.; Li, X.; Su, M.; Wang, L.; Sun, J.; Liu, Y.; Hou, L.; Yuan, C. Chemomechanically Stable Small Single-Crystal Mo-Doped $LiNi_{0.6}Co_{0.2}Mn_{0.2}O_2$ Cathodes for Practical 4.5 V-Class Pouch-Type Li-Ion Batteries. *Angew. Chem. Int. Ed.* **2023**, *62*, e202216155. [CrossRef] [PubMed]
20. Hu, Q.; He, Y.; Ren, D.; Song, Y.; Wu, Y.; Liang, H.; Gao, J.; Xu, G.; Cai, J.; Li, T.; et al. Targeted Masking Enables Stable Cycling of $LiNi_{0.6}Co_{0.2}Mn_{0.2}O_2$ at 4.6V. *Nano Energy* **2022**, *96*, 107123. [CrossRef]
21. Chen, Z.; Nguyen, H.-D.; Zarrabeitia, M.; Liang, H.-P.; Geiger, D.; Kim, J.-K.; Kaiser, U.; Passerini, S.; Iojoiu, C.; Bresser, D. Lithium Phosphonate Functionalized Polymer Coating for High-Energy $Li[Ni_{0.8}Co_{0.1}Mn_{0.1}]O_2$ with Superior Performance at Ambient and Elevated Temperatures. *Adv. Funct. Mater.* **2021**, *31*, 2105343. [CrossRef]
22. Xue, L.; Yao, M.; Peng, Y.; Li, Y.; Dong, Y.; Song, L.; Zhang, F.; Zhang, K.; Yu, M.; Cheng, F. Solvent Anchored Electrolytes for Lithium-Ion Batteries Working at High Voltage and Wide Temperature. *Angew. Chem. Int. Ed.* **2026**, *65*, e2731926. [CrossRef] [PubMed]

23. Khormali, A. Using a New Mixture of Reagents for Effective Inhibition of Corrosion and Salt Precipitation. *J. Chem. Pet. Eng.* **2021**, *55*, 257–276. [CrossRef]
24. Luo, J.; Guo, B.; Li, N.; Huang, Q.; Wang, J.; Fu, Y.; Jia, L.; Zhang, X.; Hou, J.; Zhu, J.; et al. Conductive Binary Li Borate Glass Coating for Improved Ni-Rich Positive Electrode in Sulfide-Based All-Solid-State Li Batteries. *Nat. Commun.* **2025**, *16*, 9462. [CrossRef] [PubMed]
25. Zhao, Z.; Zhang, B.; Cheng, L.; Liu, Z.; Liu, Y.; Su, S.; Ming, L.; Zhang, J.; Ou, X. Enhanced Electrochemical and Structural Stability of Ni-Rich Cathode Material by Lithium Metaborate Coating for Lithium-Ion Batteries. *ChemElectroChem* **2022**, *9*, e202101395. [CrossRef]
26. Kim, T.-H.; Moon, J.H.; Shin, J.; Mohamed, S.A.; Kim, J.; Kang, H.; Lee, Y.; Kang, H.; Cho, E. Prevention of Surface and Bulk Degradation of Co-Free Ni-Rich Layered Cathodes by Primary-Particle-Level Li_2SO_4 Coating. *J. Power Sources* **2025**, *649*, 237390. [CrossRef]
27. Chen, C.; Li, M.; Ren, X.; Zhou, M.; Xu, Q.; Yan, K. A Bifunctional Bis(Trimethylsilyl) Sulfate Additive Improved the Inorganic-Rich Solid Electrolyte Interphase for Lithium Metal Batteries. *Nano Lett.* **2025**, *25*, 8080–8088. [CrossRef] [PubMed]
28. Kim, K.; Kim, T.; Song, G.; Lee, S.; Jung, M.S.; Ha, S.; Ha, A.R.; Lee, K.T. Trimethylsilyl Compounds for the Interfacial Stabilization of Thiophosphate-Based Solid Electrolytes in All-Solid-State Batteries. *Adv. Sci.* **2023**, *10*, 2303308. [CrossRef] [PubMed]
29. Su, Y.; Chen, G.; Chen, L.; Li, L.; Li, C.; Ding, R.; Liu, J.; Lv, Z.; Lu, Y.; Bao, L.; et al. Clean the Ni-Rich Cathode Material Surface with Boric Acid to Improve Its Storage Performance. *Front. Chem.* **2020**, *8*, 573–583. [CrossRef] [PubMed]
30. Ding, H.B.; Su, Y.; Wang, X.L.; Hu, Y.; Li, X.; Zhang, H.B.; Liu, G.X.; Yu, W.S.; Dong, X.T.; Wang, J.X.; et al. Enhancing the cycling stability of nickel-rich oxide cathode materials through a multifunctional CeO_2 coating. *J. Colloid Interface Sci.* **2025**, *687*, 118–130. [CrossRef] [PubMed]
31. Yang, H.; Gao, R.; Zhang, X.; Liang, J.; Meng, X.; Lu, Z.; Cao, F.; Ye, H. Building a Self-Adaptive Protective Layer on Ni-Rich Layered Cathodes to Enhance the Cycle Stability of Lithium-Ion Batteries. *Adv. Mater.* **2022**, *34*, 2204835. [CrossRef] [PubMed]
32. Lin, F.; Fan, H.Q.; Wang, Z.Y.; Ke, C.H.; Chen, Q.; Zhang, X.D.; Ye, H.; Yang, H.; Zheng, Z.J. In Situ-Constructed Elastomeric Interphase for Grain Boundary Stabilization in High-Voltage Layered Oxide Cathodes. *Adv. Mater.* **2026**, e74129. [CrossRef] [PubMed]
33. Huang, K.; Zhou, J.; Yang, H.; Xie, T.; Lan, T.; Ong, S.; Jiang, H.; Zeng, Y.; Guo, H.; Zhang, Y. TiO_2—LiF composite coating for improving NCM622 cathode cycling stability: One-step construction. *RSC Adv.* **2023**, *13*, 33905. [CrossRef] [PubMed]
34. Neudeck, S.; Mazilkin, A.; Reitz, C.; Hartmann, P.; Janek, J.; Brezesinski, T. Effect of Low–Temperature Al_2O_3 ALD Coating on Ni–Rich Layered Oxide Composite Cathode on the Long-Term Cycling Performance of Lithium-Ion Batteries. *Sci. Rep.* **2019**, *9*, 5328. [CrossRef] [PubMed]
35. Haust, J.; Guo, Y.; Belz, J.; Ahmed, S.; Adeli, N.; Huppe, F.; Erhard, L.C.; Mereacre, V.; Rohrer, J.; Hansen, A.-L.; et al. $LiNbO_3$ Coatings on NCM622: Structure and Performance Insights. *Adv. Mater. Interfaces* **2025**, *12*, e00590. [CrossRef]
36. Yang, S.; Lv, H.; Wang, Y.; Guo, X.; Zhao, L.; Li, H.; Zhi, C. Regulating Exposed Facets of Metal-Organic Frameworks for High-Rate Alkaline Aqueous Zinc Batteries. *Angew. Chem. Int. Ed.* **2022**, *61*, e202209794. [CrossRef] [PubMed]
37. He, T.; Kang, X.; Wang, F.; Zhang, J.; Zhang, T.; Ran, F. Capacitive Contribution Matters in Facilitating High Power Battery Materials toward Fast-Charging Alkali Metal Ion Batteries. *Mater. Sci. Eng. R Rep.* **2023**, *154*, 100737. [CrossRef]

Disclaimer/Publisher's Note: The statements, opinions and data contained in all publications are solely those of the individual author(s) and contributor(s) and not of MDPI and/or the editor(s). MDPI and/or the editor(s) disclaim responsibility for any injury to people or property resulting from any ideas, methods, instructions or products referred to in the content.